Potential impact of climate change on the Intra-Americas Sea: Part-1. A dynamic downscaling of the CMIP5 model projections

CrossMark

Yanyun Liu [a,b,*], Sang-Ki Lee [a,b], David B. Enfield [a], Barbara A. Muhling [a,c], John T. Lamkin [c], Frank E. Muller-Karger [d], Mitchell A. Roffer [e]

[a] Cooperative Institute for Marine and Atmospheric Studies, University of Miami, Miami, FL, USA
[b] Atlantic Oceanographic and Meteorological Laboratory, NOAA, Miami, FL, USA
[c] Southeast Fisheries Science Center, NOAA, Miami, FL, USA
[d] College of Marine Science, University of South Florida, St Petersburg, FL, USA
[e] Roffer's Ocean Fishing Forecasting Service, Melbourne, FL, USA

ARTICLE INFO

ABSTRACT

This study examines the potential impact of anthropogenic greenhouse warming on the Intra-Americas Sea (IAS, Caribbean Sea and Gulf of Mexico) by downscaling the Coupled Model Intercomparison Project phase-5 (CMIP5) model simulations under historical and two future emission scenarios using an eddy-resolving resolution regional ocean model. The simulated volume transport by the western boundary current system in the IAS, including the Caribbean Current, Yucatan Current and Loop Current (LC), is reduced by 20-25% during the 21st century, consistent with a similar rate of reduction in the Atlantic Meridional Overturning Circulation (AMOC). The effect of the LC in the present climate is to warm the Gulf of Mexico (GoM). Therefore, the reduced LC and the associated weakening of the warm transient LC eddies have a cooling impact in the GoM, particularly during boreal spring in the northern deep basin, in agreement with an earlier dynamic downscaling study. In contrast to the reduced warming in the northern deep GoM, the downscaled model predicts an intense warming in the shallow ($\leq$200 m) northeastern shelf of the GoM especially during boreal summer since there is no effective mechanism to dissipate the increased surface heating. Potential implications of the regionally distinctive warming trend pattern in the GoM on the marine ecosystems and hurricane intensifications during landfall are discussed. This study also explores the effects of 20th century warming and climate variability in the IAS using the regional ocean model forced with observed surface flux fields. The main modes of sea surface temperature variability in the IAS are linked to the Atlantic Multidecadal Oscillation and a meridional dipole pattern between the GoM and Caribbean Sea. It is also shown that variability of the IAS western boundary current system in the 20th century is largely driven by wind stress curl in the Sverdrup interior and the AMOC.

© 2015 Elsevier B.V. All rights reserved.

1. Introduction

The Intra-Americas Sea (IAS) refers to semi-enclosed waters of the western tropical Atlantic Ocean including the Gulf of Mexico (GoM) and Caribbean Sea (CBN). The Coupled Model Inter-comparison Project phase-5 (CMIP5) climate model simulations project that the sea surface temperatures (SSTs) in the IAS may increase more than 2 °C during the 21st century due to the increasing greenhouse gas (GHG) emissions (Liu et al., 2012). The increased SSTs in the IAS may substantially affect the physical and biogeochemical properties of the seawater, with important consequences for marine ecosystems.

Many Atlantic tuna species spawn in the IAS, including Atlantic bluefin tuna (BFT). The spawning of BFT has been recorded predominantly in the

northern deep GoM from April to June (AMJ), with the optimal spawning temperature of 24 - 28 °C (e.g., Muhling et al., 2010; Schaefer, 2001). Adult BFT are adversely affected by warm water (>28 °C) and thus avoid warm features in the GoM such as the Loop Current (LC; Blank et al., 2004). In an effort to understand possible impacts of climate change on such spawning habitat, Muhling et al. (2011) analyzed the CMIP phase-3 (CMIP3) climate model simulations for the 21st century, and suggested that areas in the northern deep GoM with high probabilities of BFT larval occurrence could be almost entirely gone by the end of the 21st century. This was primarily due to increased upper ocean temperatures.

Coral reefs in the IAS are also sensitive to increasing upper ocean temperature (Hoegh-Guldberg, 1999). The increasing SSTs in tropical oceans have triggered mass coral bleaching and mortality events since the early 1980s (Baker et al., 2008; Hoegh-Guldberg et al., 2007). For instance, the record breaking warm upper ocean temperatures in the Caribbean Sea in the summer of 2005 persisted for many weeks, and

* Corresponding author at: Atlantic Oceanographic and Meteorological Laboratory, NOAA, 4301 Rickenbacker Causeway, Miami, FL 33149, USA. Tel.: +1 305 361 4538.
E-mail address: Yanyun.Liu@noaa.gov (Y. Liu).

produced the most severe and extensive mass coral-bleaching event ever recorded in the region. The repeated coral bleaching events in the Caribbean Sea since the 1980's have been broadly attributed to anthropogenic climate change (Eakin et al., 2010; van Hooidonk et al., 2013; van Hooidonk et al., submitted for publication).

In boreal summer and fall, the IAS hosts a large body of warm surface water known as the Atlantic warm pool (Lee et al., 2007; Wang et al., 2006), which affects the southerly flow of moisture into much of North America, alters the Caribbean Low-Level Jet (Wang and Lee, 2007) and plays a critical role in hurricane intensification (e.g., Wang et al., 2008). Previous studies have shown that hurricanes can rapidly intensify when they pass over the LC and spin-off warm eddies (Goni and Trinanes, 2003; Shay et al., 2000). Thus, it is important to understand how the upper ocean thermal features in the IAS may change in the 21st century, in order to predict future hurricane activity (e.g., Enfield and Cid-Serrano, 2010; Lee et al., 2011a).

The ocean circulation in the IAS is an integral part of the North Atlantic western boundary current system, and is also an important upper ocean pathway of the AMOC (Schmitz and Richardson, 1991). The western boundary current system in the IAS consists of the Caribbean Current, Yucatan Current, and Loop Current (LC), and transports mass, heat, salt and biogeochemical properties from the CBN to the North Atlantic via the GoM. To resolve the IAS western boundary current system, an eddy resolving (~10 km resolution) ocean model is needed (Chassignet et al., 2005; Li and Misra, 2014; Oey et al., 2005). However, the CMIP5 climate models have typical spatial resolutions of about 1°, which is too coarse to represent the strength, position and eddy shedding characteristics of the LC (Oey et al., 2005). Therefore, Liu et al. (2012) downscaled the CMIP3 model simulations for the 21st century using a high-resolution ocean model with a horizontal resolution of 0.1° over the GoM and CBN using CMIP3 projections as its initial and boundary conditions and surface flux forcing. The downscaled model predicted that the LC would be reduced by 20-25% during the 21st century. Liu et al. (2012) further showed that the reduced LC and associated weakening of warm LC eddies have a cooling impact in the GoM, particularly in the northern deep basin, while the low-resolution CMIP3 climate models underestimate the reduction of LC and its cooling effect, thus producing more 21st century warming than in the high-resolution experiment.

Here, we further explore the potential impact of GHG-induced warming on the IAS using a high-resolution regional ocean model constrained with the surface flux fields, initial and boundary conditions obtained from the CMIP5 model simulations under the historical, Representative Concentration Pathways 4.5 (RCP4.5), and 8.5 (RCP8.5) scenarios (Taylor et al., 2012). In order to quantify the uncertainty in our CMIP5 downscaled model projections, we also explore the 20th century warming and natural climate variability in the IAS because the GHG-induced SST increase in the IAS could be amplified or reduced due to natural variability. For example, Fig. 1 shows the total and detrended sea surface temperature (SST) anomalies in the northern GoM (100°W-82°W, 25°N-30°N) from 1870-2013 obtained from the Hadley centre global sea ice and sea surface temperature (HadISST) dataset. The observed SST anomalies in the northern GoM during the 20th century show long-term variability consistent with the Atlantic Multidecadal Oscillation (AMO). The amplitude of this multi-decadal signal is as large as 0.5 °C, which is comparable to the GHG-induced SST increase in the GoM by the 2030s (Liu et al., 2012). The 20th century warming and climate variability in the IAS are explored using a high-resolution regional ocean model forced with observed surface flux fields for the period of 1871-2008. The potential implications of anthropogenic and natural changes in the IAS on tuna spawning, coral bleaching and hurricane activities are discussed. Effects of environmental variability and change on BFT and skipjack tuna (SKJ: *Katsuwonus pelamis*) are also discussed in more depth in a companion paper (Muhling et al., in this issue).
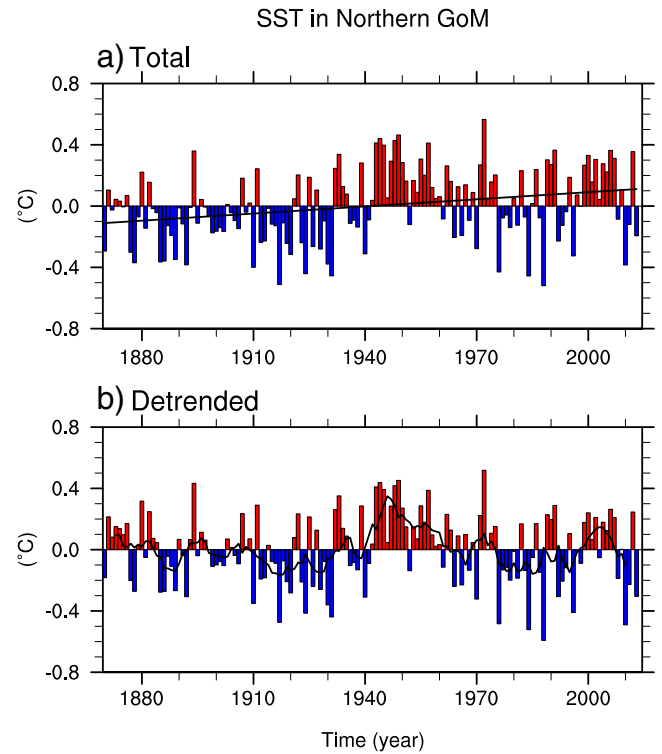

Fig. 1. (a) Total and (b) detrended SST anomaly in the northern GoM (100°W-82°W, 25°N-30°N) during 1870-2013 obtained from the HadISST dataset. The black line in Fig. 1a shows the linear trend. The black line in Fig. 1b is obtained by performing a 7-month running average to the time series of detrended SST anomaly. The unit for the temperature is °C.

2. Model and model experiments

The NOAA Geophysical Fluid Dynamics Laboratory (GFDL) Modular Ocean Model version 4.1 (MOM4; Griffies et al., 2004; Gnanadesikan et al., 2006) is used as the downscaling model in this study. The regional MOM4 model domain covers the Atlantic Ocean between 100°W and 20°E bounded north and south by 65°N and 20°S, respectively. The high-resolution MOM4 has the fully eddy-resolving horizontal resolution of 0.1° over the GoM and CBN region (10°N ~ 30°N; 100°W ~ 70°W), decreasing linearly to 0.25° in the rest of the model domain. The MOM4 has 25 vertical z-coordinate levels. To examine the impact of anthropogenic and natural climate variability on the IAS, three MOM4

Table 1
The weight of each CMIP5 model used to derive the surface flux fields and initial and boundary conditions for the MOM4 simulations.

Rank	Model	Model Weight
1	NCAR-CCSM4	2.38
2	IPSL-CM5A-LR	2.10
3	BCC-CSM1-1	1.90
4	MRI-CGCM3	1.52
5	IPSL-CM5A-MR	1.48
6	CSIRO-Mk3-6-0	1.43
7	GFDL-ESM2G	1.16
8	GISS-E2-R	1.09
9	HadGEM2-CC	0.93
10	GFDL_ ESM2M	0.68
11	HadGEM2-ES	0.65
12	CanESM2	0.55
13	MIROC-ESM	0.53
14	MIROC-ESM-CHEM	0.52
15	MIROC5	0.36
16	GFDL-CM3	0.35
17	CNRM-CM5	0.33
18	NorESM1-M	0.02

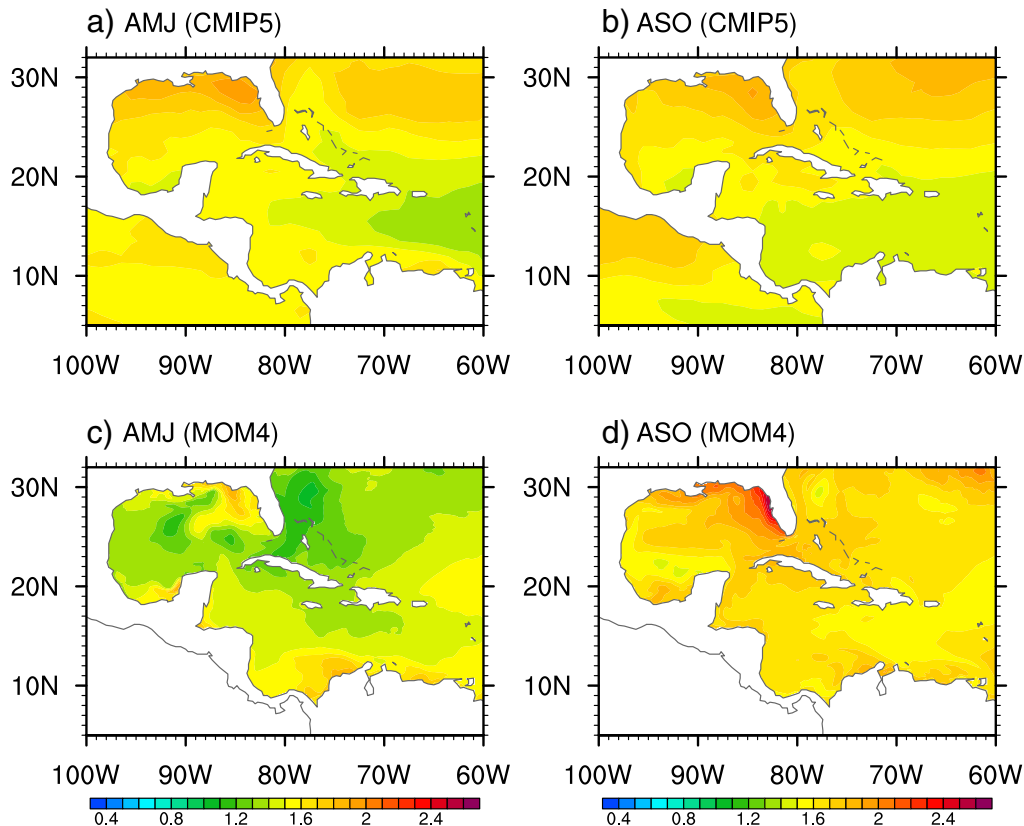## SST difference between late 20C and late 21C (RCP4.5)

Fig. 2. SST difference in the IAS between the late 21st century (2090 ~ 2098) and late 20th century (1990 ~ 1998) for (a) the boreal spring months of AMJ and (b) the boreal summer months of ASO obtained from the weighted ensemble of 18 CMIP5 models simulations under the historical and RCP4.5 scenario, (c) and (d) are same as (a) and (b), except that the SST differences are obtained from the high-resolution MOM4 experiment (EXP_HIS and EXP_4.5). The unit for the temperature is °C.

experiments (EXP_HIS, EXP_4.5 and EXP_8.5) are performed to down-scale the CMIP5 simulations under historical and two future emission scenarios, and one MOM4 experiment (EXP_20CR) is performed to simulate the 20th century climate variability and quantify the role of natural variability.

2.1. Dynamic downscaling of CMIP5 model simulations under RCP4.5 and 8.5 scenarios

For the 21st century climate change experiments, the MOM4 is driven by the monthly surface forcing fields obtained from the CMIP5 dataset (Taylor et al., 2012), including near surface wind speed, surface air temperature, sea level pressure, surface specific humidity, downwelling shortwave and longwave radiation, and precipitation. The CMIP5 model data are downloaded from the CMIP5 webpage (http://cmip-pcmdi.llnl.gov/cmip5) for the historical and two future emission scenarios. The "historical" runs are forced by observed atmospheric composition changes that include both anthropogenic and natural climate variability. The future (21st century) simulations are obtained from projections for the RCP4.5 and RCP8.5 scenarios, which represent the medium-low and high GHG emission scenarios, respectively (Taylor et al., 2012).

A total of eighteen CMIP5 models under the historical, RCP4.5, and RCP8.5 scenarios are used to derive the surface forcing fields, initial and boundary conditions. These eighteen CMIP5 models are selected because they all show a realistic AMOC strength in the 20th century and contain all surface flux variables needed for the model experiments. If there are multiple ensemble members available for any given model,

we only use the first ensemble member in our analysis. Each of the eighteen CMIP5 models is ranked and weighted based on its ability to replicate the observed annual mean upper ocean temperature at the surface, 100 m and 200 m in the GoM and CBN for the last 30 years of the 20th century (1971-2000), following Liu et al. (2012). Additionally, since the upper ocean temperature in the IAS depends strongly on the AMOC for its effect on the northward advection of warm surface water through the Yucatan Channel (e.g., Schmittner, 2005), the AMOC strength based on the maximum overturning stream function at 30°N is computed for each CMIP5 model during 1971-2000, compared to the observed value of 18.0 ± 2.5 Sv (Lumpkin and Speer, 2007), and used to rank and weight the CMIP5 models. The same weight is given for all four indices (i.e., three temperature levels and AMOC).

In order to minimize the biases in the surface forcing fields obtained from the CMIP5 model simulations, we first construct the CMIP5 climatology for the 1971-2000 periods under the historical scenario, and then compute the difference between the weighted ensemble of CMIP5 climatology and the observed surface forcing climatology. The Coordinated Ocean Research Experiments version-2 (CORE2) surface flux product (Large and Yeager, 2009) is used to derive the observed surface forcing climatology. Then, the difference (i.e., the bias-correction term) is added to the CMIP5 surface forcing fields under historical, RCP4.5 and RCP8.5 scenarios for the period of 1900-2098. To incorporate the impact of atmospheric noise on the surface fields, in each model year, the bias-corrected monthly CMIP5 surface fields are combined with randomly selected daily anomalous surface fields of CORE2 during the period of 1971-2000 following the methodology used in Lee et al. (2011b). The initial and boundary conditions for the temperature and salinity are

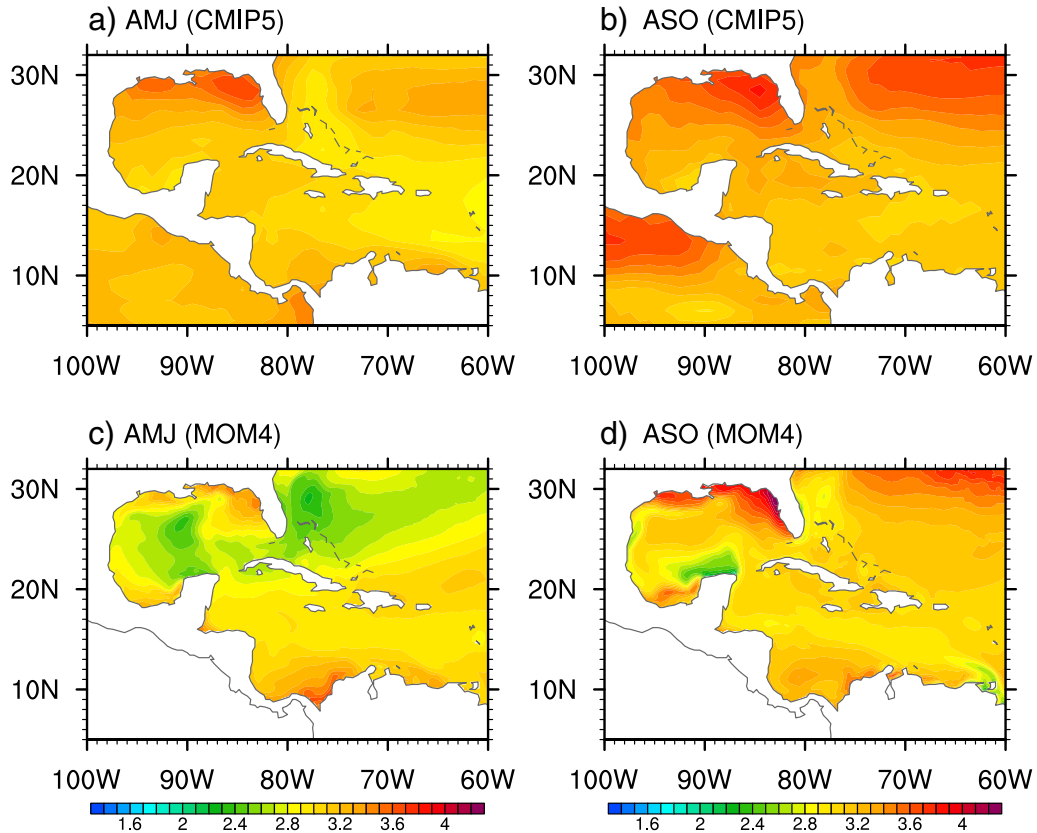## SST difference between late 20C and late 21C (RCP8.5)

Fig. 3. Same as Fig. 2 except that the SST differences are obtained from the weighted ensemble mean of CMIP5 model simulations under the historical and RCP8.5 scenarios and from EXP_HIS and EXP_8.5. The unit for the temperature is °C. The SST increase is more severe under RCP8.5 scenario and in EXP_8.5.

also bias-corrected following the same methodology used for the surface forcing fields. The observed temperature and salinity climatology are obtained from the U.S. Navy Generalized Digital Environmental Model version 3.0 (GDEM3, Carnes, 2009). The difference between the CMIP5 climatology and the observed (GDEM3) temperature and salinity climatology during the period of 1971-2000 is added to the CMIP5 temperature and salinity under the three (historical, RCP4.5, and RCP8.5) scenarios for the period of 1900 to 2098.

The weight coefficients are applied to the bias-corrected surface forcing fields, initial and boundary conditions of each CMIP5 model (see Table 1) under historical, RCP4.5, and RCP8.5 scenarios. Then, their weighted ensemble averages are derived and used to perform the MOM4 experiments. In all model experiments, the ocean boundaries at 65°N and 20°S are treated as closed, but are outfitted with about 5° of buffer zones in which the temperature and salinity are linearly relaxed toward the corresponding CMIP5 fields. Two additional buffer zones
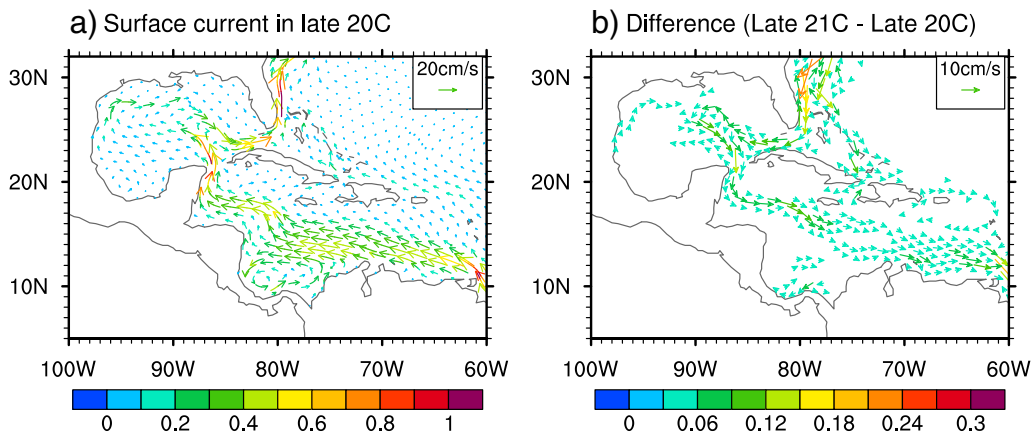
MOM4: Surface Current

Fig. 4. (a) Long-term averaged annual mean surface current obtained from EXP_HIS in the late 20th century (1990 ~ 1998). (b) Simulated surface current changes (i.e., late 21st century to late 20th century) in the IAS between the late 21st century (2090 ~ 2098) and the late 20th century obtained from EXP_HIS and EXP_8.5. The unit for the surface current is cm/s.
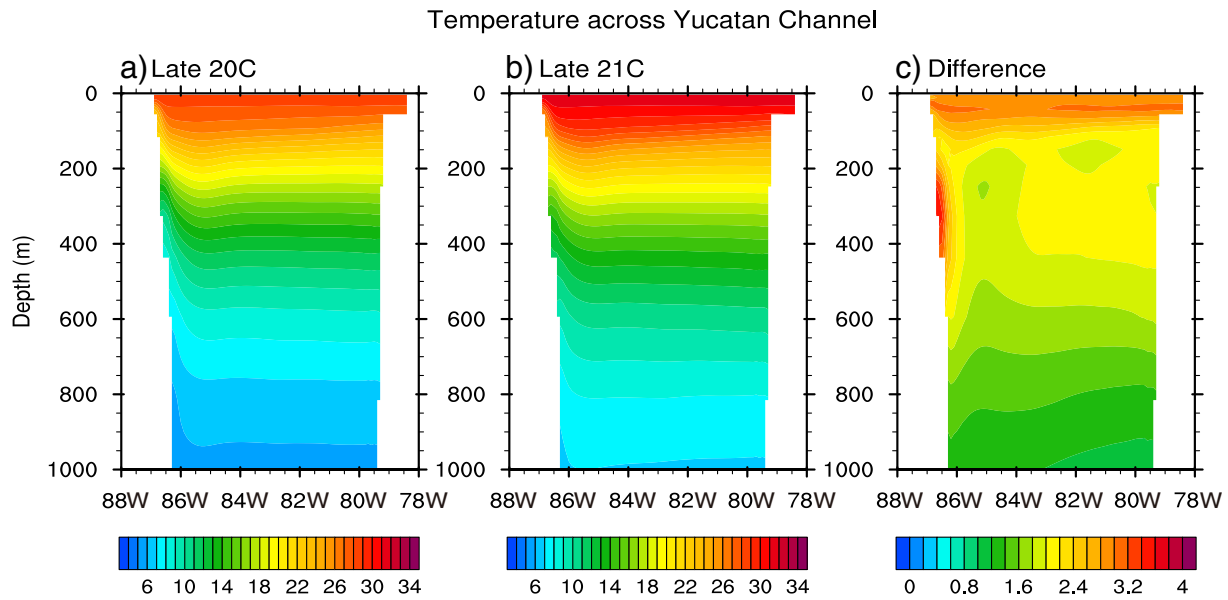
Temperature across Yucatan Channel

Fig. 5. The vertical section of long-term averaged annual mean temperature across the Yucatan Channel at 21°N during (a) the late 20th century, (b) the late 21st century, and (c) the temperature changes between late 21st century and late 20th century obtained from EXP_HIS and EXP_8.5. The unit for temperature is °C.

are located in the northwestern corner over the Labrador Sea, and in the Gulf of Cadiz (representing the Mediterranean Sea) as in Chassignet et al. (1996). The restoring time scale for the northern and southern boundaries varies linearly from 25 days at the inner edge to 5 days at the walls. The timescale for the Labrador Sea region is 25 days and, for the Mediterranean Sea, 365 days. The MOM4 simulation is initialized and integrated for 106 years using the biased-corrected CMIP5 surface forcing fields, initial and boundary conditions under the historical scenario for the period of 1900-2005 (EXP_HIS). Then the MOM4 simulations for future scenarios are continuously run from 2006 to 2098 using the bias-corrected CMIP5 surface forcing fields and boundary conditions under the RCP4.5 (EXP_4.5) and RCP8.5 (EXP_8.5) scenarios.

2.2. High-resolution ocean model simulation for the 20th century

For the 20th century model experiment, the MOM4 domain, resolution and configuration are the same as those used for the CMIP5 downscaling experiments, except that the MOM4 is driven by different surface forcing, initial and boundary conditions. The surface forcing fields are obtained from the 20th Century Reanalysis version 2 (20CR) dataset, which contains the 6-hourly surface flux variables at 2° spatial resolution spanning 1871-2008 (Compo et al., 2011). The initial and boundary conditions are derived from the Simple Ocean Data Assimilation version 2.2.6 (SODA 2.2.6) product (Giese and Ray, 2011). The surface forcing, initial and boundary conditions for the 20th century experiment are

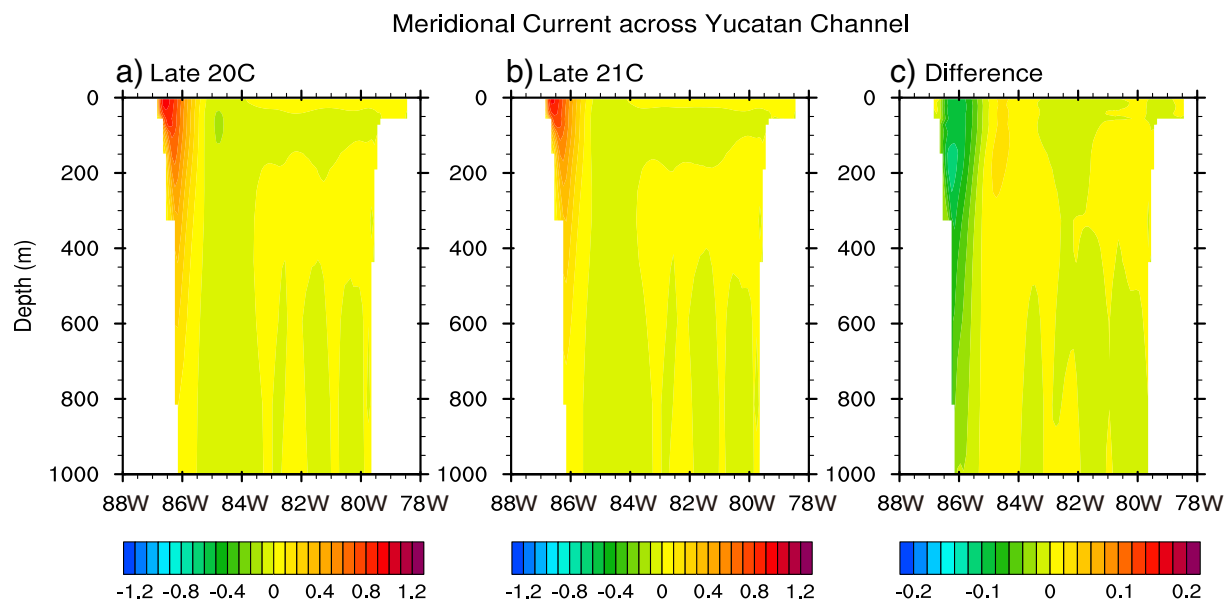## Meridional Current across Yucatan Channel

Fig. 6. The vertical section of long-term averaged annual mean meridional velocity across the Yucatan Channel at 21°N during (a) the late 20th century, (b) the late 21st century, and (c) the meridional velocity changes between late 21st century and late 20th century obtained from EXP_HIS and EXP_8.5. The unit for current is m/s.
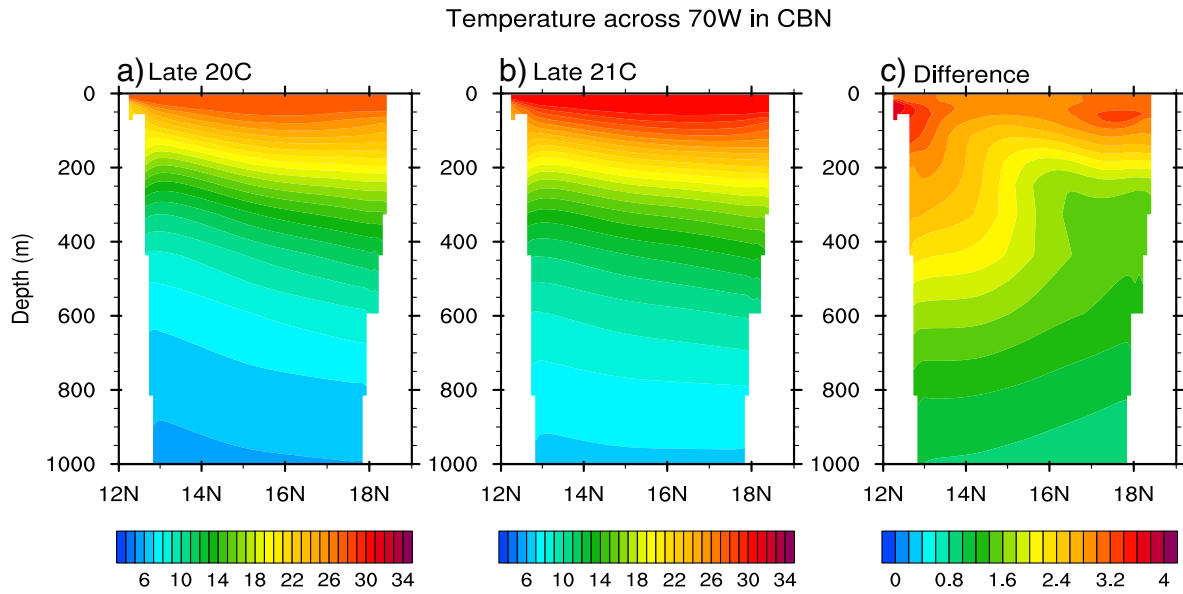
Temperature across 70W in CBN

Fig. 7. The meridional section of long-term averaged annual mean temperature across the 70°W in the CBN during (a) the late 20th century, (b) the late 21st century, and (c) the temperature changes between late 21st century and late 20th century obtained from EXP_HIS and EXP_8.5. The unit for temperature is °C.

also bias-corrected following the same methodology used for the CMIP5 downscaling experiments. The 20th century simulation (EXP_20CR) is integrated for 138 years for the period of 1871-2008. The first 30 years of model outputs are discarded to exclude any potentially spurious spin-up effect.

3. Results

3.1. GHG-induced warming pattern of the IAS in the 21st century

Fig. 2 shows the SST differences in the IAS between the late 21st century (2090 ~ 2098) and the late 20th century (1990 ~ 1998) for the boreal spring months of April, May and June (AMJ) and the boreal summer months of August, September and October (ASO) obtained

from the weighted ensemble mean of CMIP5 model simulations under the historical and RCP4.5 scenarios and from EXP_HIS and EXP_4.5. Fig. 3 is similar to Fig. 2 except that the SST differences are obtained from the weighted ensemble mean of CMIP5 model simulations under the historical and RCP8.5 scenarios and from EXP_HIS and EXP_8.5.

The CMIP5 models project that the IAS is warmed by 1.2 ~ 2 °C (3 °C or more) under the RCP4.5 (RCP8.5) scenario for both AMJ and ASO. The warming is particularly large in the northern deep GoM, which is the known spawning ground for BFT. In the MOM4 simulations, the IAS also shows extensive warming (Fig. 2c, Fig. 3c). However, the spatial pattern of the warming is quite different from the CMIP5 model projections, especially in AMJ. For AMJ, the simulated SST increase in the northern deep GoM is only about 1.4 °C (2.8 °C) in EXP_4.5 (EXP_8.5), much less than the CMIP5 SST increase of 1.8 °C (3.4 °C) under the
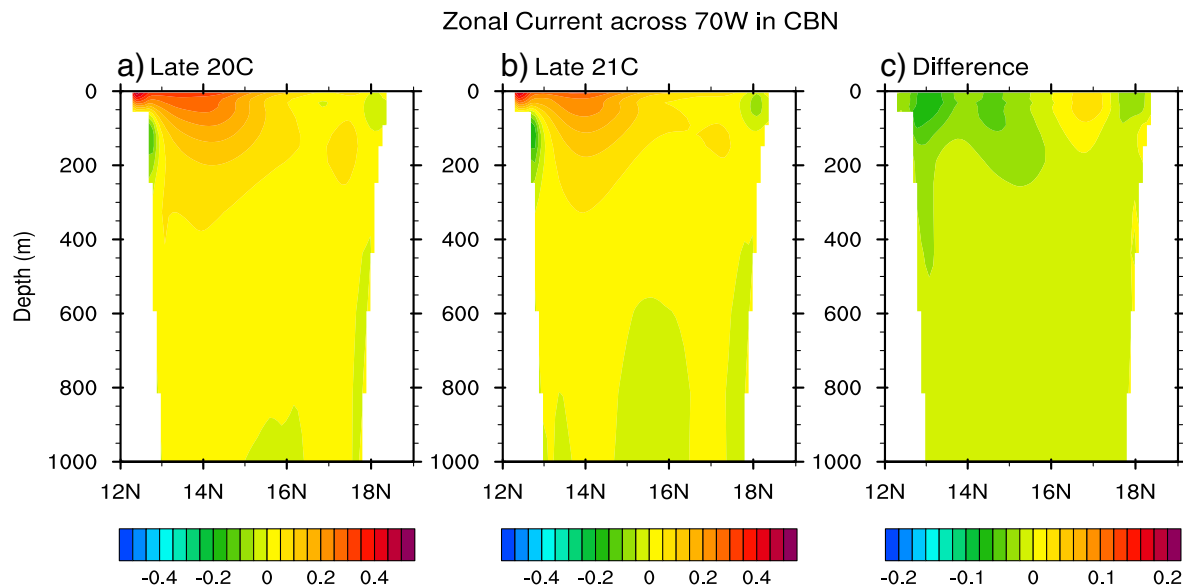
Zonal Current across 70W in CBN

Fig. 8. The meridional section of long-term averaged annual mean zonal current across the 70°W in the CBN during (a) the late 20th century, (b) the late 21st century, and (c) the zonal current changes between late 21st century and late 20th century obtained from EXP_HIS and EXP_8.5. The zonal current is positive westward. The unit for current is m/s.
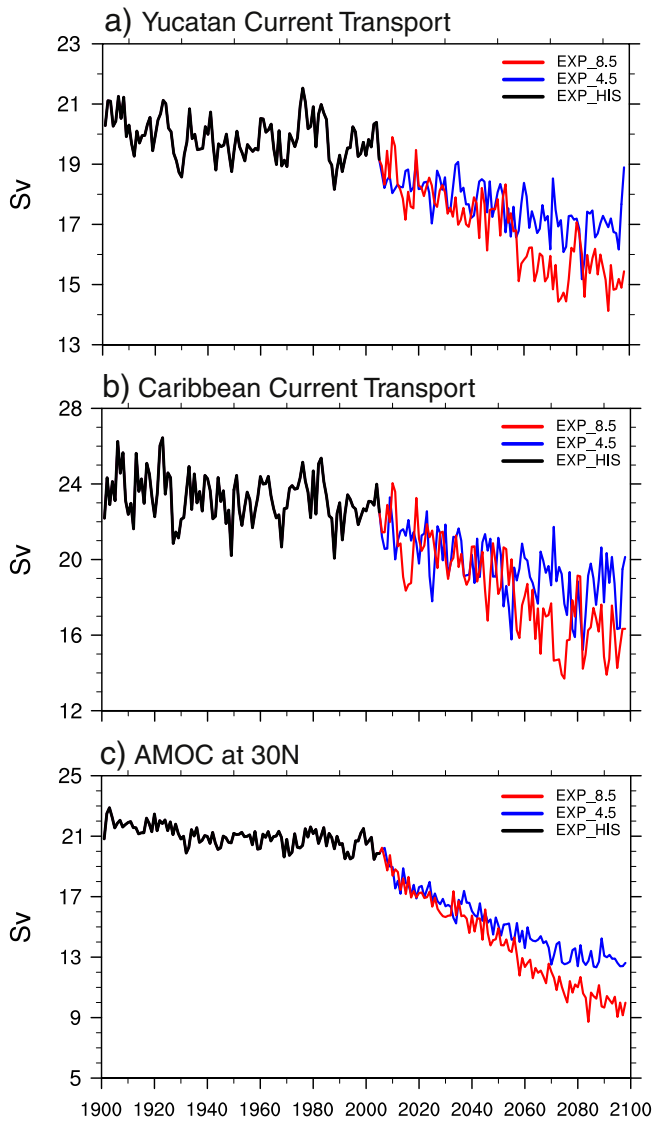
Fig. 9. (a) Time series of the simulated annual mean volume transport (Sv) across the Yucatan Channel and (b) Caribbean Current volume transport (Sv) for the period 1900-2098 obtained from EXP_HIS, EXP_4.5 and EXP_8.5. (c) Time series of the simulated AMOC (Sv) at 30°N for the period 1900-2098 obtained from EXP_HIS, EXP_4.5 and EXP_8.5.

Fig. 10. Time-averaged Atlantic MOC in the late 20th century obtained from (a) EXP_HIS, and the late 21st century obtained from (b) EXP_4.5 and (c) EXP_8.5. The unit is Sv.

RCP4.5 (RCP8.5) scenario. In fact, the northern deep GoM is characterized as the region of minimum warming in EXP_4.5 and EXP_8.5, whereas it is the region of maximum warming in the CMIP5 model projections. The SST increases in the western GoM and Straits of Florida region are also much reduced compared to the CMIP5 SST increases (Fig. 2c, Fig. 3c). A potential cause for this difference between the CMIP5 and downscaling projections is the weakening of the LC and the associated reduction in the warm water transport through the Yucatan Channel, which are not well simulated in low-resolution models such as the CMIP5 models (Liu et al., 2012).

Fig. 4a shows the long-term averaged annual surface currents obtained from EXP_HIS in the late 20th century. Fig. 4b shows the simulated surface current changes in the IAS between the late 21st century and the late 20th century obtained from EXP_HIS and EXP_8.5. The surface current differences (Fig. 4b) are clearly against the mean direction of the western boundary current system in the IAS (Fig. 4a), indicating a much-weakened LC during the late 21st century. The warm transient LC eddies detached from the main branch of the LC are also weakened, and thus shallower (not shown). The effect of the LC in the
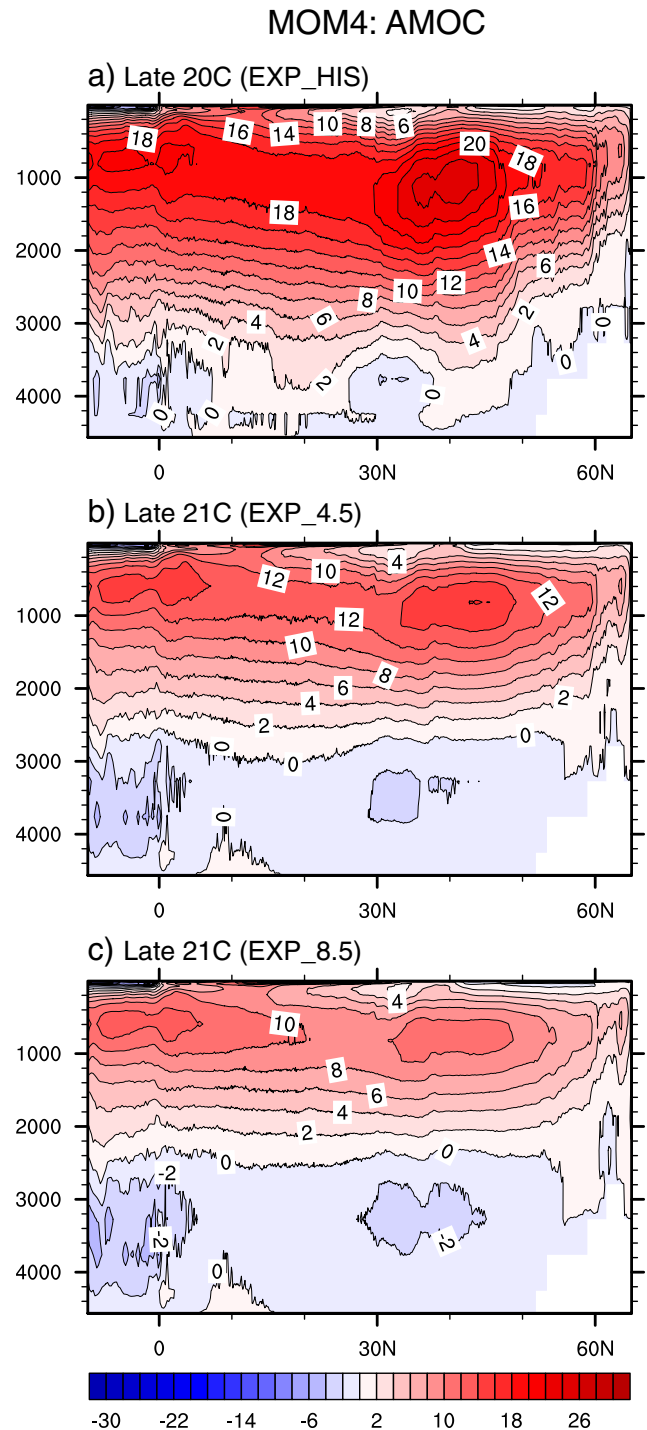
present climate is to warm the GoM (Chang and Oey, 2010; Jayne and Marotzke, 2002). Therefore, the reduced LC and the associated weakening of the warm transient LC eddies have a cooling impact in the GoM. It appears that the cooling effect is particularly large in the northern deep basin during AMJ, in agreement with the previous result from the CMIP3 downscaling simulation (Liu et al., 2012). In particular, Liu et al. (2012) performed a heat budget analysis to show that the reduced LC is mainly responsible for the reduced warming in the northern deep GoM during AMJ.

Figs. 5 and 6 show the simulated vertical section of temperature and meridional velocity across the Yucatan Channel in the late 20th century,
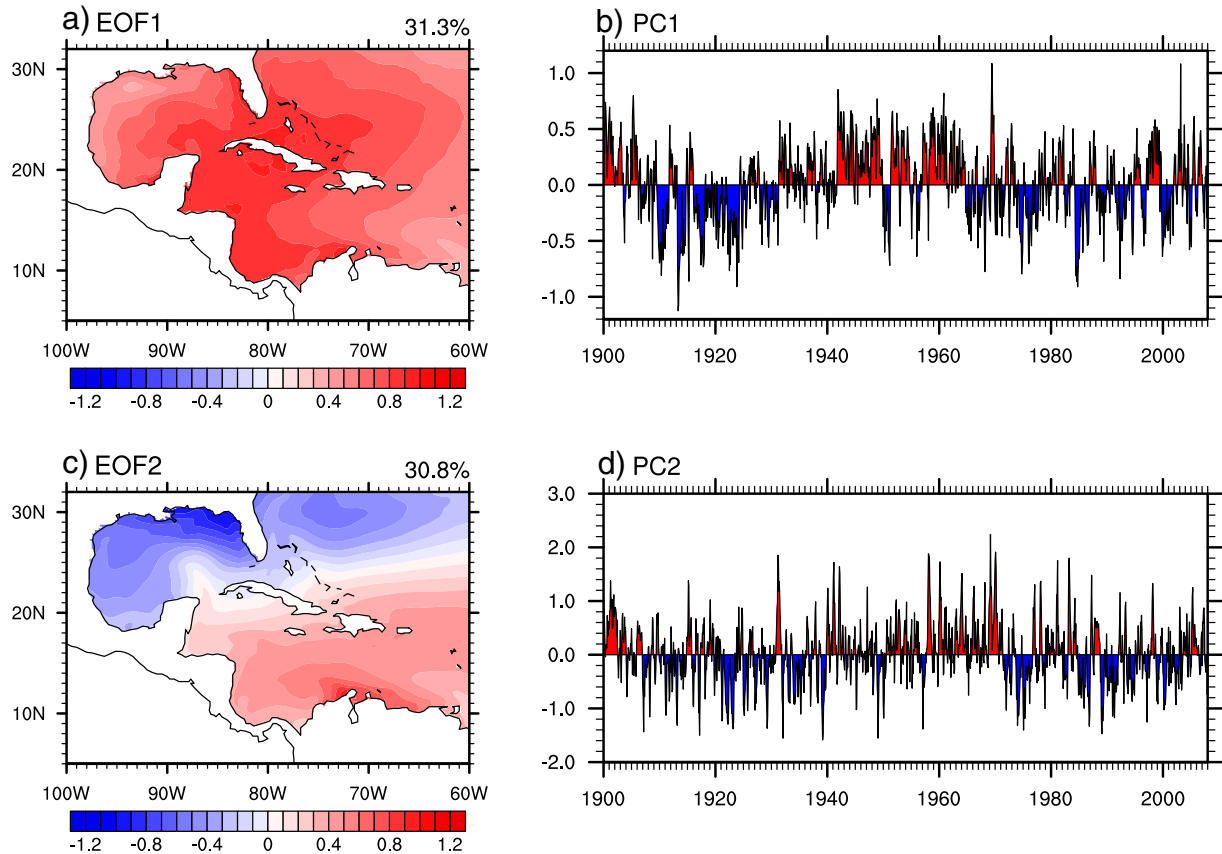
MOM4: EOF Analysis of SST (1900:2008)

Fig. 11. The two leading EOF modes of the detrended monthly SST anomalies and associated time series obtained from EXP_20CR. (a) The 1st mode (EOF1), and (b) the associated normalized time series (PC1), (c) the 2nd mode (EOF2), and (d) the associated normalized time series (PC2) during 1900-2008. The two leading modes account for 31.3% (EOF1) and 30.8% (EOF2) of the total variance, respectively. These first two EOF modes are significant at the 95% confidence level based on the criterion of North et al. (1982).

the late 21st century, and the changes between late 21st century and late 20th century obtained from EXP_HIS and EXP_8.5. As shown in Fig. 5, the simulated temperature increase across the Yucatan Channel is about 3 °C in the upper 100 m. This temperature warming is reduced in the deeper layers (i.e. ~2 °C temperature increase in the 200 - 400 m and ~1.2 °C temperature increase in the 800-1000 m). Consistent with the reduced LC, the meridional velocity across the Yucatan Channel is largely reduced during the late 21st century, mainly in the western side of the Yucatan Channel (Fig. 6).

In contrast to the reduced warming in the northern deep GoM during the boreal spring (AMJ), the downscaled model predicts an intense warming in the shallow (≤200 m) northeastern shelf of the GoM (i.e., the Louisiana-Texas Shelf and the West Florida Shelf) especially during the boreal summer (ASO). As shown in Fig. 2d, the projected SST increase in the northeastern Gulf coast for ASO is about 2.5 °C (4.0 °C) in EXP_4.5 (EXP_8.5), while the CMIP5 SST increase is only about 2.0 °C (3.5 °C) under the RCP4.5 (RCP8.5) scenario. In the shallow (≤200 m) northeastern shelf of the GoM, the surface ocean circulation is quite weak and dynamically detached from the LC in the deep GoM (due to a strong potential vorticity gradient across the continental slope). Therefore, the increased surface heating over the shallow northeastern shelf of the GoM cannot be dissipated by vertical mixing with the deeper ocean or by horizontal advection of the relatively cooler interior ocean. During other seasons, however, frequent penetration of the cold front could cool down this region. Therefore, it is highly likely that the increased summertime warming in the shallow northeastern Gulf is due to the lack of effective mechanism to dissipate the projected increase of the surface heating. The enhanced summertime warming

over the northeastern shelf of the GoM could greatly increase the chance for rapid intensification of hurricanes making landfall across the northeastern Gulf coast in the 21st century.

The downscaled MOM4 simulations also project intense summertime warming along the South American coast in the southern Caribbean Sea, which may lead to more frequent coral bleaching events in the 21st century. Figs. 7 and 8 show the meridional section of temperature and zonal velocity across the 70°W in the CBN during the late 20th century, the late 21st century, and the changes between late 21st century and late 20th century obtained from EXP_HIS and EXP_8.5. The intense warming off the South American coast (Fig. 7) is linked to the relaxation of the thermocline slope across the Caribbean Current (CC), and thus is linked to the reduced CC (Fig. 8).

The downscaled MOM4 simulations indicate that the projected reductions of the LC and CC in the 21st century play important roles in the regional warming pattern in the IAS. Therefore, it is important to understand what processes are responsible for the projected reductions of the LC and CC. Fig. 9a shows the time series of the simulated annual mean volume transport across the Yucatan Channel for the period of 1900-2098 obtained from EXP_HIS, EXP_4.5 and EXP_8.5. The volume transport across the Yucatan Channel is reduced drastically from 20 Sv during the late 20th century to 17 Sv (15 Sv) in EXP_4.5 (EXP_8.5) during the 21st century. The reduction is about 25% of the mean under the RCP8.5 scenario. The CC is also reduced from 23 Sv during the late 20th century to 19 Sv (16 Sv) for EXP_4.5 (EXP_8.5) during the late 21st century (Fig. 9b). As shown in Fig. 9c, the AMOC at 30°N is significantly reduced during the 21st century under both scenarios. Fig. 10 further shows that the AMOC is highly reduced at all latitudes by the

late 21st century (Cheng et al., 2013; Liu et al., 2012). Since the western boundary current system in the IAS, including the LC and CC, is an important pathway of the AMOC, it is likely that the reduced LC and CC in EXP_4.5 and EXP_8.5 are driven by the future deceleration of the AMOC in agreement with Liu et al. (2012).

3.2. The 20th century climate variability in the IAS

As discussed earlier, the observed SST anomalies in the northern GoM during the 20th century show long-term variability consistent with the AMO (e.g., Muller-Karger et al., 2015), and thus should be taken into account in quantifying uncertainty in our CMIP5 downscaled model projection for the 21st century. Therefore, to explore the effects of 20th century warming and climate variability in the IAS, a high-resolution regional ocean model is forced with observed surface flux fields for the period of 1871-2008 (EXP_20CR).

Fig. 11 shows the two leading Empirical Orthogonal Function (EOF) modes of the detrended monthly SST anomalies and associated time series obtained from EXP_20CR. The two leading modes account for 31.3% (EOF1) and 30.8% (EOF2) of the total variance, respectively, and are significantly separated from each other (North et al., 1982). The first mode of SST variability in the IAS is characterized by a multidecadal oscillation (Fig. 11b). The time series for EOF1 (PC1) is significantly (95% or above based on a student-*t* test) correlated with the AMO index (*r* ~ 0.76, see Fig. 12a), which is linked to climate and extreme weather variability over the North Atlantic Ocean and the surrounding continents (e.g., Enfield et al., 2001; Goldenberg et al., 2001; Ting et al., 2011; Zhang and Delworth, 2006). The AMO index is computed from

EXP_20CR, and is defined as the detrended area-averaged SST anomalies over the North Atlantic (e.g., Enfield et al., 2001).

The second EOF mode of IAS SST variability (Fig. 11c) corresponds to a meridional dipole pattern with negative SST anomalies in the GoM and positive SST anomalies in the CBN, which is a part of the well-known North Atlantic tripole mode (e.g., Deser et al., 2010). The IAS dipole has been observed in the spring following strong and persistent ENSO events (e.g., Alexander and Scott, 2002; Lee et al., 2008) and in the spring prior to anomalously large or small summer Atlantic warm pools (Enfield et al., 2006; Munoz et al., 2010). To explore why the dipole pattern prevails in the spring, the amplitude of PC2 SST anomalies for each calendar month is calculated from EXP_20CR (Fig. 12c). Compared with the SST PC1 (Fig. 12b), the SST PC2 time series show a strong seasonality with the peak seasonal variability in February, May and April (FMA).

The large amplitude dipole SST variability in FMA is possibly due to the surface heat flux during the previous season (i.e. DJF). Thus, the surface heat flux in December, January and February (DJF) is regressed onto the PC2 time series in FMA for the period of 1900-2008 as shown in Fig. 13. It is clearly shown that the net surface heat flux anomalies (Fig. 13a) largely explain the dipole SST structure with surface cooling anomalies over the GoM and the east coast of the United States, and surface warming anomalies over the CBN. Among various components of the surface heat flux anomalies, the surface latent heat flux has a dipole pattern consistent with the net surface heat flux anomalies and a relatively larger magnitude (Fig. 13c), suggesting that the primary contribution for the dipole SST pattern in the IAS is from the surface latent heat flux. As the surface northerly wind anomalies over the GoM (Fig. 13c) bring more cold and dry air from the continental U.S.
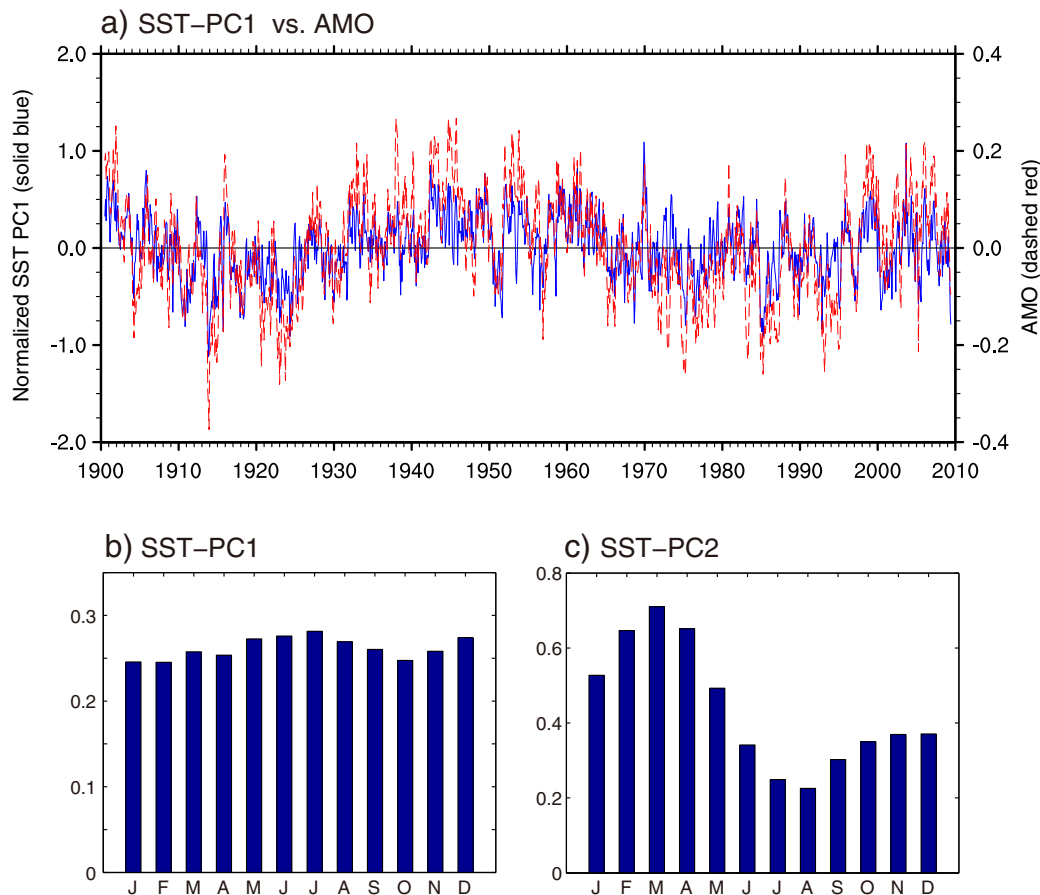

Fig. 12. (a) Time series of normalized SST-PC1 (solid blue) and AMO index (dashed red) during 1900-2008 obtained from EXP_20CR. The correlation between the AMO index and the time series of SST PC1 is 0.76, which is significant at 95% confidence level. The average magnitude of SST anomaly of (b) PC1 and (c) PC2 for each month obtained from EXP-20CR.

to the GoM, the air-sea temperature and moisture differences could lead to surface latent cooling over the GoM. Over the CBN, the surface westerly wind anomalies associated with the dipole SST pattern lead to the weakening of the easterly winds and surface latent cooling, and thus warm the CBN. The reduced easterly winds could also reduce the upwelling along the South American coast in the CBN (Fig. 13c), which may interact with the CC and further contribute to the warming in the CBN as suggested in Lee et al. (2007). The radiative heat fluxes (shortwave plus longwave radiation, Fig. 13b) also contribute positively to the dipole SST pattern in the IAS. The sensible heat fluxes (Fig. 13d) play a minor role in the GoM.

Given the important role played by the western boundary current system in the regional warming pattern of the IAS for the 21st century, the 20th century variability of the volume transport across the Yucatan Channel is examined using EXP_20CR. Fig. 14a shows the time series of the total volume transport across Yucatan Channel for the period of 1900-2008 obtained from EXP_20CR. The mean transport during 1971-2000 is about 19 Sv, which is smaller than the observed estimate of 23.8 ± 1 Sv for the period of September 1999 through June 2000 (e.g., Sheinbaum et al., 2002). Note that the volume transport across the Yucatan Channel exhibits low-frequency variability at the multidecadal time scale. The total volume transport across the Yucatan Channel is divided into three components: the wind-driven gyre component, the AMOC component, and the residual. In the classical theories of wind-driven ocean circulation (e.g., Munk, 1950; Stommel, 1948), the interior Sverdrup transport is balanced by the compensating transport within the western boundary. Therefore, the wind-driven component of the volume transport across the Yucatan Channel is estimated by integrating the wind-stress curl from the eastern boundary to the western boundary along the latitude of Yucatan Channel (21°N) then flipping the sign.

Partial linear regression in the context of multiple linear regression analysis is used here for the decomposition. Here, the total volume transport across the Yucatan Channel is reconstructed as a function of the wind-driven gyre component (V_{GYRE}) and the AMOC component (V_{MOC}). The total volume transport across the Yucatan Channel can be written as

$$V_{YC} = a \cdot V_{GYRE} + b \cdot V_{MOC} + c, \tag{1}$$

where a (0.20), b (0.45) and c (3.14) are partial regression coefficients, and V_{MOC} is defined as the maximum overturning stream function at 30°N. Partial linear regression is an effective tool to regress (or predict) one dependent variable using multiple independent variables (or predictors) when the independent variables are not orthogonal to each other (e.g., Ryan, 2009). The main concept of partial linear regression is very similar to that of partial correlation because it gives the amount of increase in the dependent variable with respect to the unit increase in one independent variable while all other independent variable are held constant. For instance, the partial regression coefficient of V_{YC} on V_{GYRE} (i.e., a in Eq. (1)) is the amount of increase in V_{YC} with respect to the unit increase in V_{GYRE} while V_{MOC} is held constant.
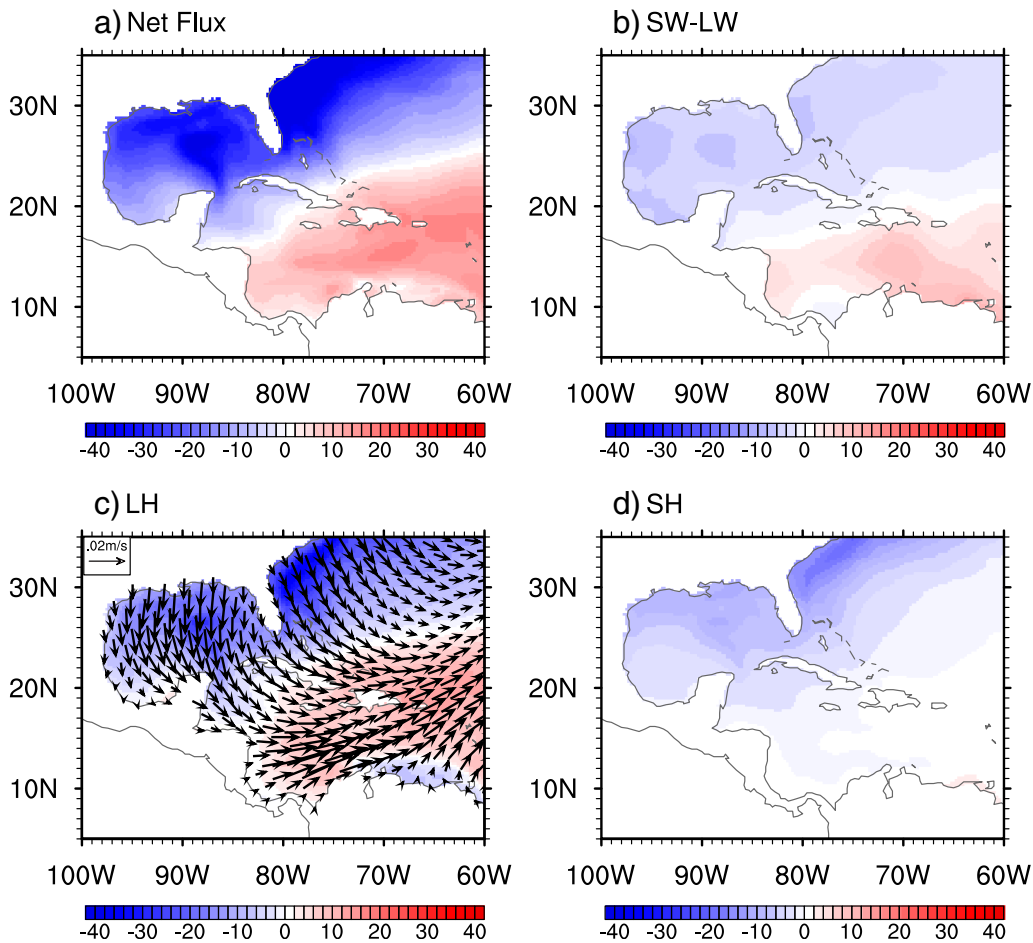

Fig. 13. Monthly surface heat flux in DJF regressed onto the SST PC2 time series in FMA for the period of 1900-2008, obtained from the EXP_20CR. (a) Net heat flux, (b) Radiation heat fluxes (shortwave plus longwave radiation), (c) Latent heat flux (color) overlaid with wind stress (vector), and (d) Sensible heat flux. The unit for the heat flux terms is W/m². All the flux terms are positive downward.
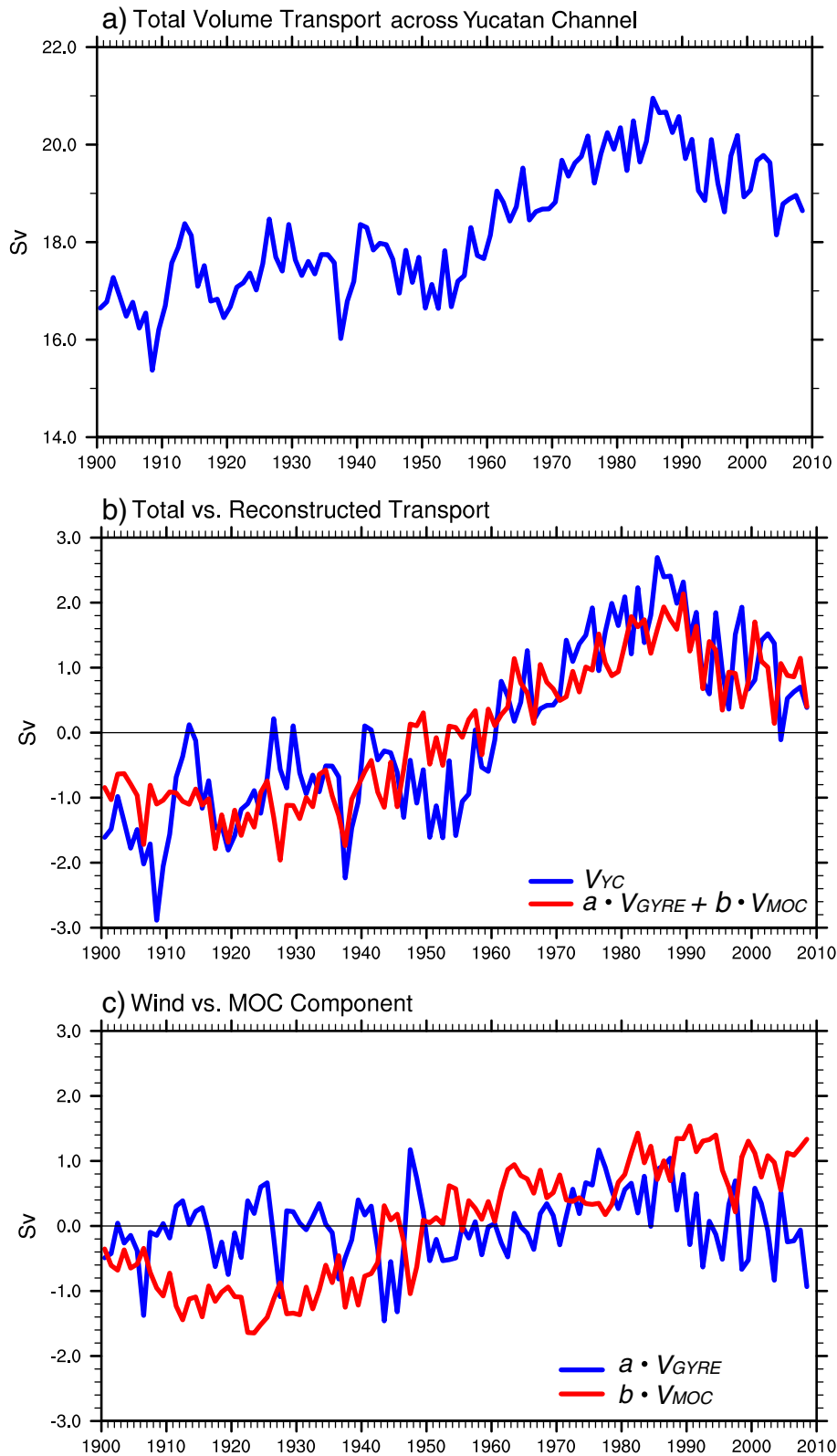
a) Total Volume Transport across Yucatan Channel

b) Total vs. Reconstructed Transport

c) Wind vs. MOC Component

Fig. 14. (a) Time series of the total volume transport across Yucatan Channel for the period of 1900 - 2008 obtained from EXP_20CR, (b) time series of the total (V_{YC}, blue) and reconstructed volume transport (red) during 1900-2008, and (c) time series of wind-driven gyre component ($a \cdot V_{GYRE}$, blue) and the AMOC component ($b \cdot V_{MOC}$, red) during the 1900-2008 obtained from EXP_20CR. The mean value of the total volume transport across the Yucatan Channel in Fig. 9b and c has been subtracted for concise. V_{MOC} is defined as the maximum overturning stream function at 30°N. The unit is Sv.

Fig. 14b shows the time series of the total (V_{YC}) and reconstructed volume transport during the 20th century. Fig. 14c shows the wind-driven gyre component ($a \cdot V_{GYRE}$) and the AMOC component ($b \cdot V_{MOC}$). The reconstructed volume transport is expressed as the first two terms on the RHS of (1) (i.e., $a \cdot V_{GYRE} + b \cdot V_{MOC}$). The reconstructed volume transport is significantly correlated ($r = 0.83$)

with the total transport, and both show an increasing trend during the 20th century. As shown in Fig. 14c, the AMOC component ($b \cdot V_{MOC}$) shows a similar positive trend, and is significantly correlated with the total transport ($r = 0.72$). The positive trend of the AMOC in the 20th century has been attributed to anthropogenic aerosols (Menary et al., 2013), reduced Arctic freshwater export (Mueller et al., 2014) and increased Agulhas Current leakage augmented by the strengthening of the wind stress curl over the South Atlantic and Indian subtropical gyre (Lee et al., 2011b).

The wind-driven gyre component ($a \cdot V_{GYRE}$) does not show any trend, but is significantly correlated with the total transport ($r = 0.41$). It is interesting to note that the wind-driven gyre component ($a \cdot V_{GYRE}$) is significantly anti-correlated with the AMO ($r = -0.42$) suggesting that the wind-driven volume transport across the Yucatan Channel is reduced during a positive phase of the AMO. In summary, about 70% of the total variance of the volume transport across the Yucatan Channel during the 20th century can be explained by wind stress curl in the Sverdrup interior and the AMOC.

3.3. Basin-averaged SST increases in the GoM and CBN during the 21st century

Fig. 15a shows the time series of annual mean SST anomalies averaged over the GoM (100°W-82°W, 21°N-30°N) during 1900-2008 obtained from EXP_20CR and HadISST. Fig. 15b shows the time series of the annual mean SSTs averaged over the GoM during 1900-2098, obtained from EXP_HIS, EXP_4.5 and EXP_8.5. As shown, the annual
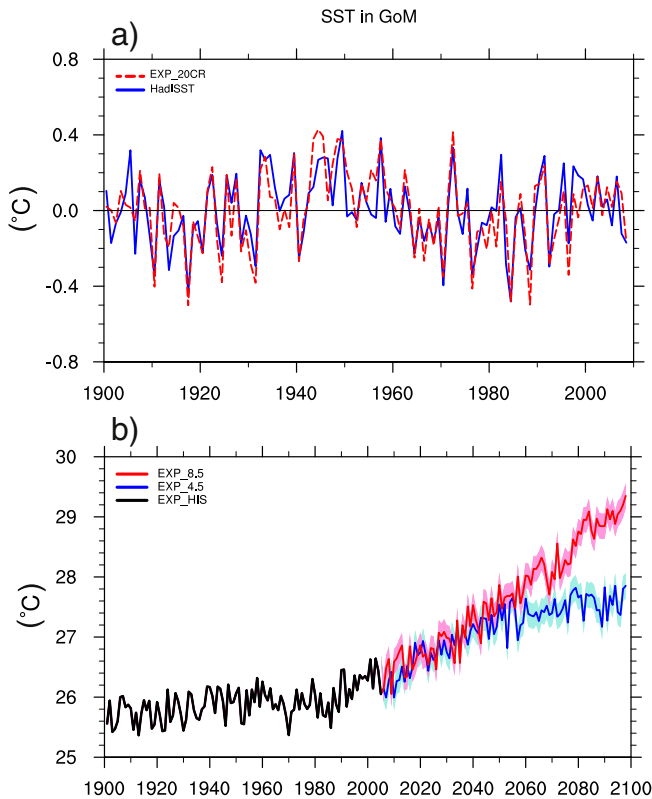
Fig. 15. (a) Time series of annual mean SST anomalies averaged over the GoM (100°W-82°W, 21°N-30°N) during 1900-2008 obtained from EXP_20CR and HadISST. (b) Time series of the annual mean SSTs averaged over the GoM during 1900-2098 obtained from EXP_HIS (black), EXP_4.5 (blue) and EXP_8.5 (red). The standard deviation (STD) of the SST anomalies in the GoM for the period of 1900-2008 (EXP_20CR) is calculated (STD = 0.21) and the ± 0.21 °C is added to each time point of the future SST projections (light color regions) obtained from EXP_4.5 and EXP_8.5. The unit is °C.
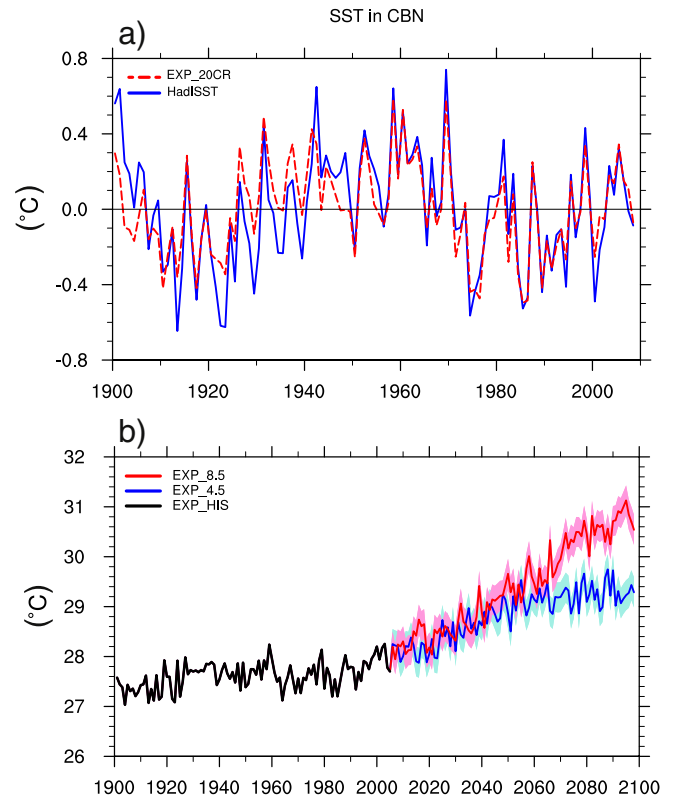
Fig. 16. Same as Fig. 15, except for the CBN (85°W-60°W, 10°N-20°N). The STD (± 0.30 °C) is added to each time point of the future SST projections (light color regions) obtained from EXP_4.5 and EXP_8.5. The unit is °C.

mean SSTs in the GoM increase about 1.5 °C (3.0 °C) under the RCP4.5 (RCP8.5) scenario between the late 20th century and the late 21st century. As indicated in Fig. 15a, the annual mean SST anomalies in the GoM during the 20th century (EXP_20CR and HadISST) display long-term variability consistent with the AMO. Assuming that the AMO-like variability in the 20th century continues throughout the 21st century, it is logical to add the AMO-like natural variability as the uncertainty in our projections for the 21st century. Thus, the standard deviation (STD) of the SST anomalies in the GoM for the period of 1900-2008 (EXP_20CR) is calculated (STD = 0.21) and added to the future projections for both scenarios (light color regions in Fig. 15b) as a measure of uncertainty in the projections. As clearly shown in Fig. 15b, the uncertainty due to natural climate variability is quite large. The GHG-induced SST increase in the GoM can be amplified or reduced due to natural SST variability in the GoM. Therefore, it is quite important to consider the uncertainty due to natural variability for the future projections of the SSTs in the GoM. On average, under RCP4.5 (RCP8.5) scenario, the GHG-induced SST increase in the GoM over a 26-year (13-year) period is statistically significant if the uncertainty due to natural variability is considered. Fig. 16a and b are the same as Fig. 15a and b, expect for the CBN (85°W-60°W, 10°N-20°N). It is clear that our conclusions drawn for the GoM are also applicable for the CBN.

4. Summary and discussion

In this study, we examine the potential impact of GHG-induced warming on the IAS by using an eddy-resolving resolution ocean model constrained with the surface forcing fields and initial and boundary conditions obtained from the CMIP5 model simulations under historical and two future scenarios (EXP_HIS, EXP_4.5 and EXP_8.5). The downscaled MOM4 simulations suggest that the simulated volume

transport by the western boundary current system in the IAS can be reduced considerably by 20-25% during the 21st century, consistent with a similar rate of projected reduction in the AMOC. The effect of the LC in the present climate is to warm the GoM. Therefore, the reduced LC and the associated weakening of the transient warm LC eddies have a cooling impact in the GoM, particularly in the northern deep GoM during AMJ. The distribution of the cooling impact is consistent with the locations of the mean LC and its transient warm eddies that propagate into the western GoM. Low-resolution models, such as the CMIP5 models, underestimate the reduction of the LC and its cooling effect, and thus fail to simulate the reduced warming in the northern deep GoM. These results are in agreement with an earlier dynamic downscaling study (Liu et al., 2012) based on a different ocean model and under different forcing (CMIP3 climate models under A1B scenario), suggesting that these results (i.e, reduced warming in the northern deep GoM) are robust.

The reduced warming of the northern deep GoM in spring will have important implications for marine ecosystems, including the spawning of BFT. Since the spawning of BFT is mainly temperature dependent and adult BFT generally avoid very warm surface waters, the reduced warming in the northern GoM may mitigate the CMIP5-projected reduction in BFT spawning grounds in the GoM (Muhling et al., in this issue). In contrast, tropical tuna species such as SKJ may benefit from future warming, through spatial and temporal expansion of spawning grounds (Muhling et al., in this issue).

In contrast to the reduced warming in the northern deep GoM, the downscaled model predicts an enhanced warming in the shallow (≤200 m) northeastern shelf of the GoM, especially during boreal summer. The enhanced warming along the northeastern shelf of the GoM could greatly increase the chance for rapid intensification of hurricanes making landfall across the northeastern Gulf coast in the 21st century. The downscaled model experiments also indicate that the southern CBN will be a region of enhanced warming yearlong. The enhanced warming along the northeastern South American coast in the western CBN may lead to an increased frequency of coral bleaching events during the 21st century.

This study also explores the 20th century warming and climate variability in the IAS using a high-resolution regional ocean model forced with observed surface flux fields (EXP_20CR). It is shown that the main modes of SST variability in the IAS are linked to the AMO and a meridional dipole pattern between the GoM and CBN. The dipole SST mode is a part of the well-known North Atlantic tripole mode. The main contributor for the dipole SST pattern is the surface latent heat flux linked to the northerly and westerly (or southerly and easterly) wind anomalies in the GoM and CBN, respectively.

The 20th century variability of the western boundary current system in the IAS is driven by both wind stress curl in the Sverdrup interior and the AMOC. The AMOC component shows an increasing trend, and is significantly correlated with the total transport ($r = 0.72$). The wind-driven gyre component does not show any trend, but is also significantly correlated with the total transport ($r = 0.41$).

It is important to point out some of the limitations in this study. Here, we use the ensemble mean from the CMIP5 models to drive the MOM4 simulations, which may reduce the internal variability within the individual models. Therefore, this work can also benefit from performing more downscaled MOM4 simulations forced by one (or more) of the individual models, especially by choosing the one or ones with the highest weights to estimate the range of temperature variability within the 21st century.

In this work, we use only a dynamic ocean model to study the potential impact of GHG-induced warming on the IAS. In the future, a regional biogeochemical ocean simulation is required to study the impact of GHG-induced warming on the ocean ecosystem in the IAS (Pastor et al., 2013). The future study will also benefit from the development of regional coupled atmosphere-ocean models (Li and Misra, 2014).

References

Alexander, M., Scott, J., 2002. The influence of ENSO on air-sea interaction in the Atlantic. Geophys. Res. Lett. 29, 1701. http://dx.doi.org/10.1029/2001GL014347.

Baker, A.C., Glynn, P.W., Riegl, B., 2008. Climate change and coral reef bleaching: An ecological assessment of long-term impacts, recovery trends and future outlook. Estuar. Coast. Shelf Sci. 80 (4), 435–471.

Blank, J.M., Morrissette, J.M., Landeira-Ferandez, A.M., Blackwell, S.B., Williams, T.D., Block, B.A., 2004. In situ cardiac performance of Pacific bluefin tuna hearts in response to acute temperature change. J. Exp. Biol. 207, 881–890. http://dx.doi.org/10.1242/jeb.00820.

Carnes, M.R., 2009. Description and evaluation of GDEM-V 3.0. Tech. Rep. 724/NRL/MR/7300–09–9165, Nav. Res. Lab., Washington, D. C. (Available at http://www7320.nrlssc.navy.mil/pubs/pubs.php)

Chang, Y.-L., Oey, L.-Y., 2010. Eddy and wind forced heat transports in the Gulf of Mexico. J. Phys. Oceanogr. 40, 2727–2742.

Chassignet, E.P., Smith, L.T., Bleck, R., Bryan, F.O., 1996. A model comparison: Numerical simulations of the North and Equatorial Atlantic oceanic circulation in depth and isopycnic coordinates. J. Phys. Oceanogr. 26, 1849–1867. http://dx.doi.org/10.1175/1520-0485(1996)026<1849:AMCNSO>2.0.CO;2.

Chassignet, E.P., Hulburt, H.E., Smedstad, O.M., Barron, C.N., Ko, D.S., Rhodes, R.C., Shriver, J.F., Wallcraft, A.J., Arnone, A.R., 2005. Assessment of data assimilative ocean models in the Gulf of Mexico using Ocean Color. Circ. Gulf Mex. Obs. Models 161, 87–100.

Cheng, W., Chiang, J.C.H., Zhang, D., 2013. Atlantic Meridional Overturning Circulation (AMOC) in CMIP5 models: RCP and historical Simulations. J. Clim. 26, 7187–7197. http://dx.doi.org/10.1175/JCLI-D-12-00496.1.

Compo, G.P., Whitaker, J.S., Sardeshmukh, P.D., Matsui, N., Allan, R.J., Yin, X., Gleason, B.E., Vose, R.S., Rutledge, G., Bessemoulin, P., Brönnimann, S., Brunet, M., Crouthamel, R.I., Grant, A.N., Groisman, P.Y., Jones, P.D., Kruk, M.C., Kruger, A.C., Marshall, G.J., Maugeri, M., Mok, H.Y., Nordli, Ø., Ross, T.F., Trigo, R.M., Wang, X.L., Woodruff, S.D., Worley, S.J., 2011. The twentieth century reanalysis project. Q. J. R. Meteorol. Soc. 137, 1–28. http://dx.doi.org/10.1002/qj.776.

Deser, C., Alexander, M.A., Xie, S.-P., Phillips, A.S., 2010. Sea surface temperature variability: patterns and mechanisms. Ann. Rev. Mar. Sci. 2, 115–143.

Eakin, C.M., et al., 2010. Caribbean corals in crisis: record thermal stress, bleaching, and mortality in 2005. PLoS ONE 5 (11), e13969. http://dx.doi.org/10.1371/journal.pone.0013969.

Enfield, D.B., Cid-Serrano, L., 2010. Secular and multidecadal warmings in the North Atlantic and their relationships with major hurricane activity. Int. J. Climatol. 30, 174–184. http://dx.doi.org/10.1002/joc.1881.

Enfield, D.B., Mestas-Nunez, A.M., Trimble, P.J., 2001. The Atlantic multidecadal oscillation and its relation to rainfall river flows in the continental U.S. Geophys. Res. Lett. 28, 2077–2080.

Enfield, D.B., Lee, S.-K., Wang, C., 2006. How are large western hemisphere warm pools formed? Prog. Oceanogr. 70 (2–4), 346–365. http://dx.doi.org/10.1016/j.pocean.2005.07.006.

Giese, B.S., Ray, S., 2011. El Niño variability in simple ocean data assimilation (SODA), 1871–2008. J. Geophys. Res. 116, C02024. http://dx.doi.org/10.1029/2010JC006695.

Gnanadesikan, A., et al., 2006. GFDL's CM2 global coupled climate models. Part II: the baseline ocean simulation. J. Clim. 19, 675–697. http://dx.doi.org/10.1175/JCLI3630.1.

Goldenberg, S.B., Landsea, C.W., Mestas-Nunez, A.M., Gray, W.M., 2001. The recent increase in Atlantic hurricane activity: causes and implications. Science 293, 474–479. http://dx.doi.org/10.1126/science.1060040.

Goni, G.J., Trinanes, J.A., 2003. Ocean thermal structure monitoring could aid in the intensity forecast of tropical cyclones. EOS Trans. Am. Geophys. Union 84 (51), 73–578.

Griffies, S.M., Harrison, M.J., Pacanowski, R.C., Rosati, A., 2004. A technical guide to MOM4. GFDL ocean group technical report No. 5. NOAA/Geophysical Fluid Dynamics Laboratory, Princeton, NJ (342 pp.).

Hoegh-Guldberg, O., 1999. Coral bleaching, Climate Change and the future of the world's Coral Reefs. Rev. Mar. Freshw. Res. 50, 839–866.

Hoegh-Guldberg, O., Mumby, P.J., Hooten, A.J., Steneck, R.S., Greenfield, P., et al., 2007. Coral reefs under rapid climate change and ocean acidification. Science 318 (5857), 1737–1742.

Jayne, S.R., Marotzke, J., 2002. The oceanic eddy heat transport. J. Phys. Oceanogr. 32, 3328–3345.

Large, W.G., Yeager, S.G., 2009. The global climatology of an interannually varying air-sea flux data set. Clim. Dyn. 33, 341–364. http://dx.doi.org/10.1007/s00382-008-0441-3.

Lee, S.-K., Enfield, D.B., Wang, C., 2007. What drives seasonal onset and decay of the Western Hemisphere warm pool? J. Clim. 20, 2133–2146. http://dx.doi.org/10.1175/JCLI4113.1.

Lee, S.-K., Enfield, D.B., Wang, C., 2008. Why do some El Ninos have no impact on tropical North Atlantic SST? Geophys. Res. Lett. 35, L16705. http://dx.doi.org/10.1029/2008GL034734.

Lee, S.-K., Enfield, D.B., Wang, C., 2011a. Future impact of differential inter-basin ocean warming on Atlantic hurricanes. J. Clim. 24, 1264–1275. http://dx.doi.org/10.1175/2010JCLI3883.1.

Lee, S.-K., Park, W., van Sebille, E., Baringer, M.O., Wang, C., Enfield, D.B., Yeager, S., Kirtman, B.P., 2011b. What caused the significant increase in Atlantic ocean heat content since the mid-20th century? Geophys. Res. Lett. 38. http://dx.doi.org/10.1029/2011GL048856 L17607.

Li, H., Misra, V., 2014. Thirty-two-year ocean–atmosphere coupled downscaling of global reanalysis over the Intra-American Seas. Clim. Dyn. http://dx.doi.org/10.1007/s00382-014-2069-9.

Liu, Y., Lee, S.-K., Muhling, B.A., Lamkin, J.T., Enfield, D.B., 2012. Significant reduction of the Loop Current in the 21st century and its impact on the Gulf of Mexico. J. Geophys. Res. 117, C05039. http://dx.doi.org/10.1029/2011JC007555.

Lumpkin, R., Speer, K., 2007. Global ocean meridional overturning. J. Phys. Oceanogr. 37, 2550–2562. http://dx.doi.org/10.1175/JPO3130.1.

Menary, M.B., Roberts, C.D., Palmer, M.D., Halloran, P.R., Jackson, L., Wood, R.A., Mueller, W.A., Matei, D., Lee, S.-K., 2013. Mechanisms of aerosol-forced AMOC variability in a state of the art climate model. J. Geophys. Res. 118, 2087–2096. http://dx.doi.org/10.1002/jgrc.20178.

Mueller, W.A., Matei, D., Bersch, M., Jungclaus, J.H., Haak, H., Lohmann, K., Compo, G.P., Sardeshmukh, P.D., Marotzke, J., 2014. A twentieth-century reanalysis forced ocean model to reconstruct the North Atlantic climate variation during the 1920s. Clim. Dyn. http://dx.doi.org/10.1007/s00382-014-2267-5.

Muhling, B.A., Lamkin, J.T., Roffer, M.A., 2010. Predicting the occurrence of bluefin tuna (*Thunnusthynnus*) larvae in the northern Gulf of Mexico: Building a classification model from archival data. Fish. Oceanogr. 19, 526–539.

Muhling, B.A., Lee, S.-K., Lamkin, J.T., Liu, Y., 2011. Predicting the effects of climate change on bluefin tuna (Thunnus thynnus) spawning habitat in the Gulf of Mexico. ICES J. Mar. Sci. 68, 1051–1062. http://dx.doi.org/10.1093/icesjms/fsr008.

Muhling, B.A., Liu, Y., Lee, S.-K., Lamkin, J.T., Roffer, M.A., Muller-Karger, F.E., Walter III, J.F., 2015. Potential impact of climate change on the Intra-Americas Sea: Part-2. Implications for Atlantic bluefin tuna and skipjack tuna adult and larval habitats. J. Mar. Syst. http://dx.doi.org/10.1016/j.jmarsys.2015.01.010 (in this issue).

Muller-Karger, F.E., Smith, J.P., Werner, S., Chen, R., Roffer, M., Liu, Y., Muhling, B., Lindo-Atichati, D., Lamkin, J., Cerdeira-Estrada, S., Enfield, D.B., 2015. Natural Variability of Surface Oceanographic Conditions in the Offshore Gulf of Mexico. Prog. Oceanogr. http://dx.doi.org/10.1016/j.pocean.2014.12.007.

Munk, W.H., 1950. On the wind-driven ocean circulation. J. Meteorol. 7, 80–93.

Munoz, E., Wang, C., Enfield, D., 2010. The Intra-Americas Sea springtime surface temperature anomaly dipole as fingerprint of remote influences. J. Clim. 23 (1), 43–56. http://dx.doi.org/10.1175/2009JCLI3006.1.

North, G.R., Moeng, F.J., Bell, T.J., Cahalan, R.F., 1982. Sampling errors in the estimation of Empirical Orthogonal Functions. Mon. Weather Rev. 110, 699–706. http://dx.doi.org/10.1175/1520-0493(1982)110<0699:SEITEO>2.0.CO;2.

Oey, L.-Y., Ezer, T., Lee, H.C., 2005. Loop Current, rings and related circulation in the Gulf of Mexico: A review of numerical models and future challenges. In: Sturges, W.,

Lugo-Fernandez, A. (Eds.), Circulation in the Gulf of Mexico: Observations and Models. Geophys. Monogr. Ser. 161. AGU, Washington, D. C., pp. 31–56. http://dx.doi.org/10.1029/161GM04.

Pastor, M.V., Palter, J.B., Pelegrí, J.L., Dunne, J.P., 2013. Physical drivers of interannual chlorophyll variability in the eastern subtropical North Atlantic. J. Geophys. Res. Oceans 118, 3871–3886. http://dx.doi.org/10.1002/jgrc.20254.

Ryan, T., 2009. Modern Regression Methods. 2nd ed. John Wiley, New Jersey (672 pp.).

Schaefer, K.M., 2001. Reproductive biology. In: Block, B.A., Stevens, E.D. (Eds.), Tunas: Physiology, Ecology and Evolution. Academic, San Diego, Calif, pp. 225–270 http://dx.doi.org/10.1016/S1546-5098(01)19007-2.

Schmittner, A., 2005. Decline of the marine ecosystem caused by a reduction in the Atlantic overturning circulation. Nature 434, 628–633. http://dx.doi.org/10.1038/nature03476.

Schmitz Jr., W.J., Richardson, P.L., 1991. On the sources of the Florida Current. Deep Sea Res. Part A 38 (Suppl. 1), S379–S409.

Shay, L., Goni, G., Black, P., 2000. Effects of a warm oceanic feature on Hurricane Opal. Mon. Weather Rev. 128, 1366–1383.

Sheinbaum, J., Candela, J., Badan, A., Ochoa, J., 2002. Flow structure and transport in Yucatan Channel. Geophys. Res. Lett. 29 (3), 1040. http://dx.doi.org/10.1029/2001GL013990.

Stommel, H., 1948. The westward intensification of wind-driven ocean currents. Trans. Am. Geophys. Union 29 (2), 202–206.

Taylor, K.E., Stouffer, R.J., Meehl, G.A., 2012. An overview of CMIP5 and the experiment design. Bull. Am. Meteorol. Soc. 93, 485–498. http://dx.doi.org/10.1175/BAMS-D-11-00094.1.

Ting, M., Kushnir, Y., Seager, R., Li, C., 2011. Robust features of Atlantic multi-decadal variability and its climate impacts. Geophys. Res. Lett. 38, L17705. http://dx.doi.org/10.1029/2011GL048712.

van Hooidonk, R., Maynard, J.A., Planes, S., 2013. Temporary refugia for coral reefs in a warming world. Nat. Clim. Chang. 3, 508–511.

van Hooidonk, R., Maynard, J.A., Liu, Y., Lee, S.-K., 2015. Downscaled projections of Caribbean coral bleaching that can inform conservation planning. Glob. Chang. Biol. (submitted for publication).

Wang, C., Lee, S.-K., 2007. Atlantic warm pool, Caribbean low-level jet, and their potential impact on Atlantic hurricanes. Geophys. Res. Lett. 34, L02703. http://dx.doi.org/10.1029/2006GL028579.

Wang, C., Enfield, D.B., Lee, S.-K., Landsea, C.W., 2006. Influences of Atlantic warm pool on western hemisphere summer rainfall and Atlantic hurricanes. J. Clim. 19, 3011–3028. http://dx.doi.org/10.1175/JCLI3770.1.

Wang, C., Lee, S.-K., Enfield, D.B., 2008. Atlantic warm pool acting as a link between Atlantic multidecadal oscillation and Atlantic tropical cyclone activity. Geochem. Geophys. Geosyst. 9, Q05V03. http://dx.doi.org/10.1029/2007GC001809.

Zhang, R., Delworth, T.L., 2006. Impact of Atlantic multidecadal oscillations on India/Sahel rainfall and Atlantic hurricanes. Geophys. Res. Lett. 33, L17712. http://dx.doi.org/10.1029/2006GL026267.